A Comparative Study on Airborne Lidar Waveform Decomposition Methods

Qinghua Li, Serkan Ural, Jie Shan
Lyles School of Civil Engineering, Purdue University
West Lafayette, IN 47907, USA
{li975, sural, jshan}@purdue.edu

***Abstract*—This paper applies pattern recognition methods to airborne lidar waveform decomposition. The parametric and nonparametric approaches are compared in the experiments. The popular Gaussian mixture model (GMM) and expectation-maximization (EM) decomposition algorithm are selected as the parametric approach. Nonparametric mixture model (NMM) and fuzzy mean-shift (FMS) are used as the nonparametric approach. We first run our experiment on simulated waveforms. The experiment setup is in favor of the parametric approach because GMM is used to generate the waveforms. We show that both parametric and nonparametric approaches return satisfying results on the simulated mixture of Gaussian components. In the second experiment, real data acquired with an airborne lidar are used. We find that NMM fits the data better than GMM because the Gaussian assumption is not well satisfied in the real dataset. Considering that the emitted signals of a laser scanner may even not satisfy the Gaussian assumption, we conclude that nonparametric approaches should generally be utilized for practical applications.**

Keywords: lidar; full waveform; waveform decomposition; mean shift; expectation-maximization.

I. INTRODUCTION

Lidar is one of the most widely used remote sensing techniques [1]. Its characteristics of high accuracy, high resolution and high speed make it desirable in many academic and industrial applications. The original data of most lidar systems is lidar waveform [2]. Waveform decomposition and georeferencing are necessary procedures to obtain the popular lidar point cloud and other lidar derivative products.

Waveform decomposition is necessary for generating high quality lidar products. Its algorithms can be classified into three categories: peak/edge detection [3][4], deconvolution [5][6], and pattern recognition [7][8]. The peak/edge detection method is the simplest approach for waveform decomposition, but it does not take overlapping waveform components into consideration. As a result, it sacrifices the intrinsic accuracy and fidelity of the advanced lidar systems. Deconvolution methods can provide better results, but they are sensitive to the noise level [5]. Some deconvolution methods require the system impulse response to be known [6], which unfortunately may not be provided by the data vendors. Pattern recognition approach models lidar waveforms as the histogram of samples of a random variable [9]. Many conventional clustering algorithms can be applied to classify these samples. One advantage of the pattern recognition approach is that more information is available in the decomposition result [10]. Not only the positions of targets but also the shapes of the waveforms can be obtained from the clustering result.

In this paper, we compare parametric and nonparametric methods as two different approaches for waveform decomposition. We use both methods to model the lidar waveforms, and compare the outcomes of corresponding algorithms.

II. WAVEFORM DECOMPOSITION APPROACHES

Both the parametric and nonparametric methods assume the lidar waveform $y(t)$ to be a sum of several waveform components $y_k(t)$, k=1, …, C. Their difference is that $y_k(t)$ in the parametric model is a specific function with parameter (set) θ, while in the nonparametric model it is a cluster of data points.

A. Parametric approach

Gaussian mixture model (GMM) is the most popular parametric model used for lidar waveforms [11]. In GMM, the lidar waveform is modeled as the sum of several Gaussian components:

$$y(t) = \sum_{i=1}^{C} w_i \cdot y_i(t) = \sum_{i=1}^{C} w_i \cdot \exp\left[-\frac{(t-\mu_i)^2}{2\sigma_i^2}\right] \quad (1)$$

where $\mu = [\mu_1, \dots, \mu_C]$ determines the positions of the waveform components, $\sigma = [\sigma_1, \dots, \sigma_C]$ controls the width of each component, and $w = [w, \dots, w_C]$ is their weights, C is the number of waveform components .

Expectation-maximization, or EM [12], is used to estimate the parameters of the mixture model. It repeatedly calculates the expectation of the classes of latent samples, and uses the maximum likelihood estimation (MLE) to estimate the parameters.

B. Nonparametric approach

In the framework of nonparametric mixture model (NMM), a lidar waveform is considered as the sum of data clusters. Each cluster is composed of a collection of data samples $\{x_n\}$:

$$y(t) = \sum_{i=1}^{C} y_i(t) = \sum_{i=1}^{C} \left[\frac{1}{N_i \times h} \sum_{n_i=1}^{N_i} w_{n_i} \cdot k\left(\frac{t-x_{n_i}}{h}\right)\right] \quad (2)$$

where k(.) is a kernel function of the model and h is the bandwidth [13].

Part of the work was supported by the Army Research Office.

The nonparametric clustering problem can be solved by the fuzzy mean-shift (FMS) algorithm [14], which determines the modes in the data and clusters all the data samples accordingly.

III. EXPERIMENTS

We evaluate the effectiveness of GMM and NMM on decomposing lidar waveforms with both simulated and real data. Firstly, GMM is used to simulate lidar waveforms. Then we apply both EM and FMS to decompose the simulated waveforms. Finally, we use both algorithms to analyze a real airborne lidar dataset.

A. Experiment with simulated data

We simulated lidar waveforms under the assumption of GMM since it is widely accepted in many waveform decomposition algorithms. In the simulation, C, μ, σ and w were given and the waveforms were generated according to equation (1). Two representative waveforms are illustrated in Fig. 1. There are one (a) and two (b) Gaussian component(s) in the waveforms respectively. The solid lines are the simulated waveforms and the dashed lines the Gaussian components. Each Gaussian component corresponds to an object detected by the lidar sensor, hence a point in the point cloud. The positions of the Gaussian components are marked as '+'. The position estimates are used to calculate the ranges between the detected objects and the lidar sensor.

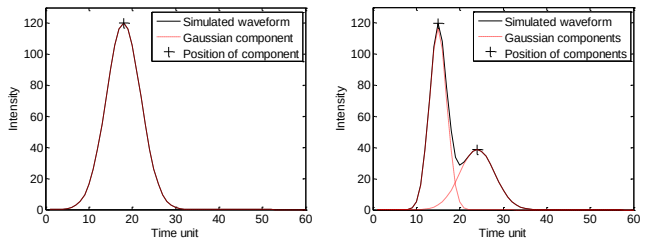

(a) (b)

Fig. 1. A simulated lidar waveform with (a) one Gaussian component; (b) two Gaussian components

A waveform decomposition algorithm should be able to estimate the following parameters: the number of waveform components C, their positions $\mu = [\mu_1, \dots, \mu_C]$, widths $\sigma = [\sigma_1, \dots, \sigma_C]$, and weights $w = [w, \dots, w_C]$. In practice, some algorithms (EM, Levenberg-Marquardt, etc.) assume that the number of waveform components, C is given. We estimated the parameters $\theta = [\mu, \sigma, w]$ with the same assumption.

Firstly, we studied the case where C=1 with an experiment. In this case, there is a single Gaussian component in the waveform. We generated 15 Gaussian waveforms, each at a random position with widths ranging from 3 to 10 in 0.5 increments. Next, we used EM and FMS to estimate the position of the waveform component. Since EM already assumes GMM, it directly estimates the Gaussian mean as the unknown position. On the other hand, FMS has no knowledge on the shape of the waveforms. It outputs the clustering result where each cluster is regarded as a waveform component. The position can be calculated by the mean or peak of the cluster. At this stage, we used both the cluster mean and peak indicated as NMM1 and NMM2 respectively to estimate the position. The estimation error is measured by $e = |\mu - \hat{\mu}|$, where μ and $\hat{\mu}$ are the position of the simulated Gaussian component and the estimated value, respectively. The errors from different approaches are summarized in Fig. 2.

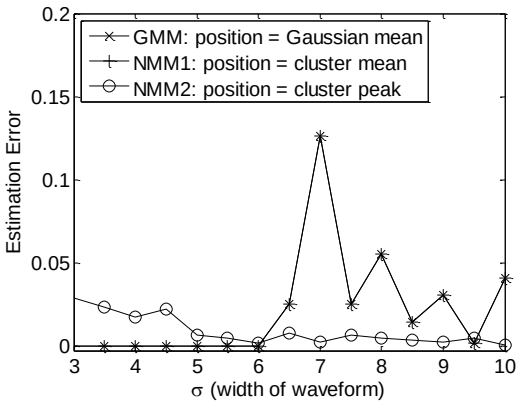

Fig. 2. Algorithm comparison on simulated waveform with one Gaussian component.

In this experiment, NMM1 returned identical results with GMM. Compared with NMM2, the estimation error of NMM1 was higher and less stable for waveform widths greater than 6. Since real lidar waveforms often have a large variation on width, NMM2 should be a better solution than NMM1. In the following experiments, we exclusively used cluster peak in NMM to estimate the position of the waveform components.

In the second experiment, we generated a sequence of waveforms, each with two Gaussian components. The following cases were studied:

- The distances between the two components were varied, while their variances and weights were fixed.
- The variance of one waveform component was changed while other parameters were fixed.
- The weights of the two components were varied while their position and variance were fixed.

We generated 10 waveforms for each case. The results with GMM and NMM (cluster peak as the position) are presented in Fig. 3. In the figures, component 1 and 2 are the first and the second waveform components received by the sensor. For each component, the estimation error with GMM and NMM is plotted. The values of fixed parameters are also listed in the caption.

In Fig. 3(a) and (b), the estimation error decreases as the distance between the two components increases and the width of the component decreases. It can be explained by the fact that the two components are more separable in such cases. In Fig. 3(c), the estimation error of NMM decreases as the weight of the first waveform component rises. It conforms the fact that we ran the mean-shift algorithm from the first component [14]. In all three plots, we find that the estimation error returned by GMM has larger variation than NMM. Finally, in most scenarios, the estimation error with either model is lower than 0.4. For a lidar system with a sampling rate of one nanosecond, such estimation error will introduce a range error of less than 6cm.

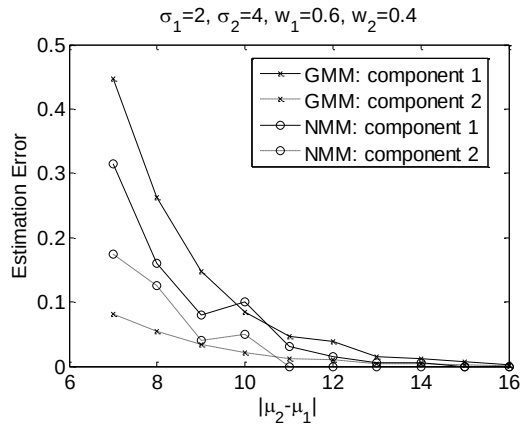

(a)

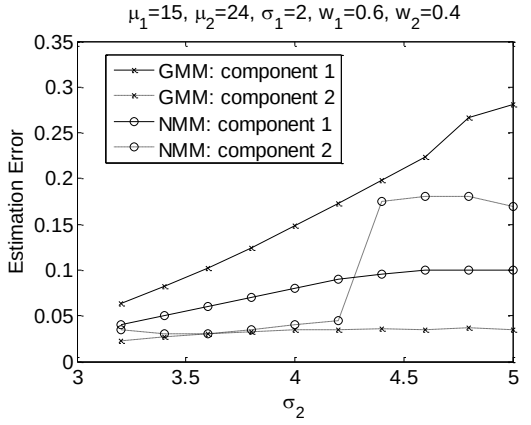

(b)

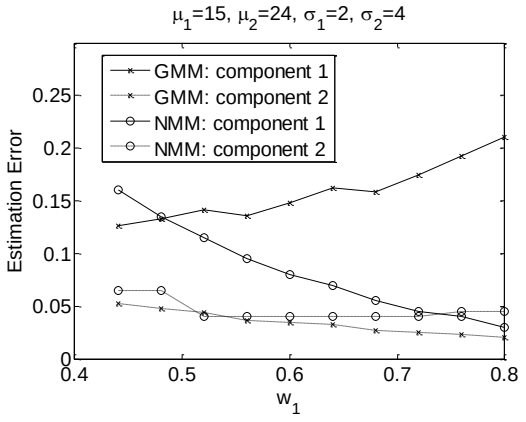

(c)

Fig. 3. Estimation error of GMM and NMM along (a) the distance between waveform components; (b) the width of a waveform component; (c) the weight of waveform components.

B. Experiment with real lidar data

The actual lidar data were collected by a Riegl Q680i airborne laser scanner. As reported in [14], the emitted signals of the scanner are overall asymmetric. Most of them are right-skewed with a mean skewness of 0.0563.

The study area is part of Shenandoah National Park, VA, USA. The whole dataset is mainly composed of two classes: bare ground and forest. For bare ground, the emitted lidar signal is directly reflected by the surface so that a single waveform component is expected in the returned waveform. For forest, the footprint of the lidar signal may cover multiple targets such as leaves, trunks and ground. The returned waveforms could be either a single component or multiple components. In other words, the number of waveform components (C) is known to be 1 for the bare ground, but unknown for the forest area. For this reason, we performed our tests on the bare ground area only.

Fig. 4. The bare ground in: (a) World Imagery of Esri, where an 10x10m^2 study area is highlighted in red; (b) Google Earth^{TM} DigitalGlobe image, where the locations of the two waveform examples are marked with blue pin icons.

We selected a 10x10m^2 area from the bare ground as highlighted in Fig. 4(a). There are altogether 5,031 waveforms in this area, so the waveform/point density is 50 per square meter. Two waveform examples are selected to study in the following experiments as pinpointed in Fig. 4(b). In the experiment, we didn't use the estimation error to evaluate the algorithms since the ground truth was not available at the time of the experiment. Instead, we checked the residuals between the original waveform and the reconstructed waveform from EM or FMS. Also, we visually checked the fitness of the two approaches.

The decomposition results of two example waveforms are plotted in Fig. 5. First, it is noted that the original lidar waveforms have a noise floor that is not introduced in the simulation. Such noise may be generated by the sensor, atmosphere or sampling and they are inevitable in real lidar data. For EM, a threshold pre-filtering was applied to remove the noise. FMS classifies such noises as 'non-informative' clusters and removes them after waveform decomposition.

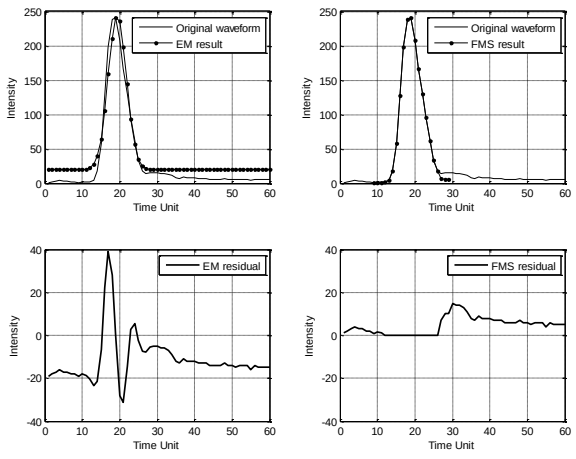

(a)

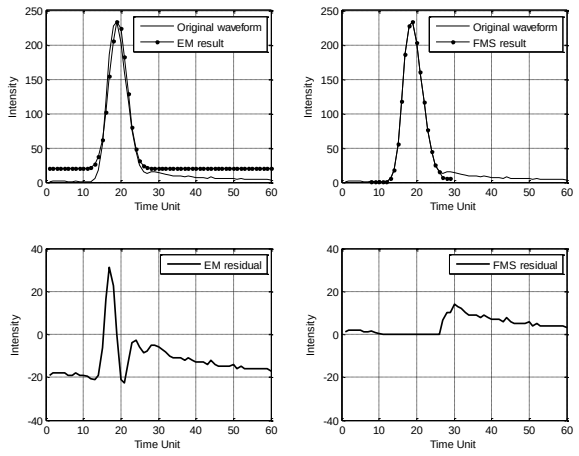

(b)

Fig. 5. Decomposition results of (a) waveform #1170908, and (b) waveform #1073866. The results with GMM are plotted on the left and that with NMM on the right.

In both Fig. 5(a) and 5(b), the decomposition results from EM is plotted on the left and the results from FMS is on the right. It can be observed that the lowest intensity of the EM decomposed component is 20, which is equivalent to the threshold in the pre-filtering process. The Gaussian component from EM obviously deviates from the original waveform, meaning that the assumption of GMM doesn't hold in this situation. As a result, the difference between the residuals of the two sides of the main component is more than 40. Increasing the number of the Gaussian components may reduce the residual deviation. However, it will generate more than one point on the ground, contradicting the fact that such waveforms are returned from the bare ground.

On the right, the results from FMS are plotted. The waveform components fit the original waveforms well, because most part of the signal falls into the main cluster. The residual of the informative component has the intensity in the range 0-15. Such residuals are clustered as non-informative clusters and removed thereafter.

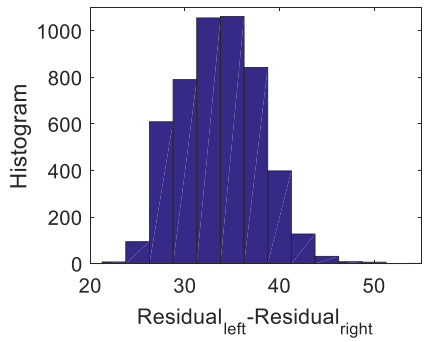

Fig. 6. Histogram of the differences of EM residuals

The two waveform examples are quite representative in our dataset. We ran EM on all the waveforms (5,031 in total) in the 10x10m^2 study area. For each waveform, we refer to the residual on the left side of the peak position as *Residual*$_{\text{left}}$, and the residual on the right side as *Residual*$_{\text{right}}$. The histogram of the residual difference, *Residual*$_{\text{left}}$-*Residual*$_{\text{right}}$, is shown in Fig. 6. Among all waveforms, 1,907 have a residual difference greater than 35. We conclude that the fitness of GMM is quite limited in the dataset.

C. Comparison with the reference DEM

The highest resolution reference dataset in the study area that was available to us at the time of the study is the DEM with 5m ground sampling distance collected by the USGS for geological studies in the Paine Run watershed. The vertical RMSE of the dataset is reported as +/-0.15 m. We generated point clouds using both EM and FMS methods from the full-waveform dataset. The area covered by the point clouds generated from the full-waveform data and the reference DEM of USGS coincide in part only. We selected the areas that intersect in all datasets for comparison as shown in Fig. 7.

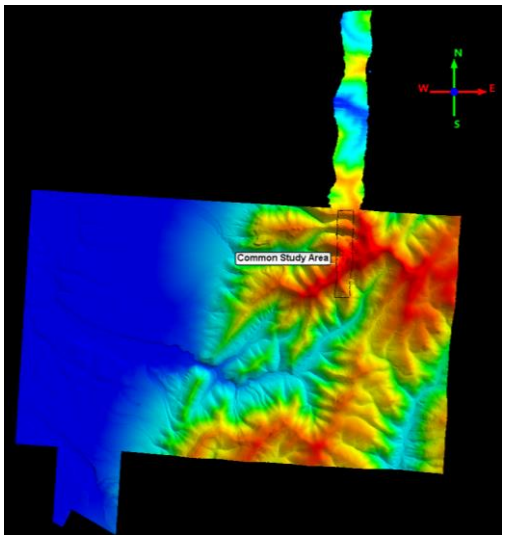

Fig. 7. Common area (black rectangular box) of the 5 m USGS DEM (large rectangular area) and the full-waveform dataset (elongated rectangular area extending from the north-east part of the USGS DEM)

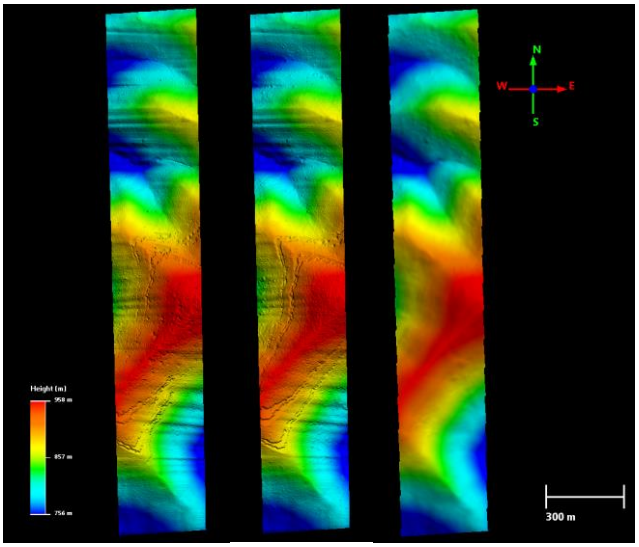

Fig. 8. DEMs with 1 m grid sampling generated with EM (left) and FMS (middle) methods, and USGS reference DEM (right) with 5 m grid sampling.

Next, we removed the off-ground points in the point clouds using the ground filtering module of LASTools software suite by applying the same set of filter parameters for both datasets. Once the ground points were obtained, we generated DEMs of 1m grid sampling from both EM and FMS ground point clouds. In Fig. 8, DEMs generated from full-waveform datasets are presented together with the reference DEM of USGS.

Full-waveform DEMs provide more details compared to the USGS DEM since the former have finer ground sampling. The reference DEM also demonstrates a smoother surface since it is documented to be generated through interactive processing by operator assistance following automatic ground filtering [15]. No such additional effort was carried out for the DEMs generated from the full-waveform lidar dataset.

Apart from the level of details, an observable difference of the full-waveform derived DEMs from the USGS DEM is the existence of repeating linear undulations on the terrain roughly in the east-west direction throughout the study area. In order to explore the magnitude of these structures as compared to the reference DEM, we first aligned the FMS and the USGS DEMs and calculated the distances between these surfaces. Discrepancies due to georeferencing are observed between the FMS DEM and the USGS DEM. We applied an Iterative Closest Point (ICP) transformation [16] to the FMS ground points to match the reference USGS DEM using CloudCompare software [17]. Then we calculated the distances between the two surfaces by calculating the distances from each point in the FMS point cloud to the best least-squares fitting planes in the USGS surface. The undulations observed in the FMS surface are clearly observed in the elevation component of the calculated distances as seen in Fig. 9. Other areas where deviations from the USGS DEM are observed include the discontinuities in the terrain and where the USGS DEM is smoother at the depression on the terrain.

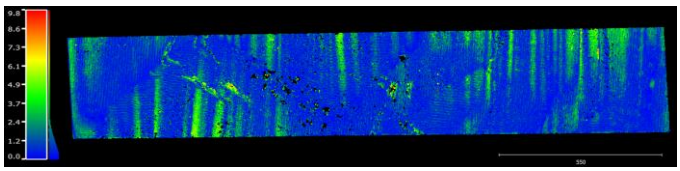

Fig. 9. Elevation component of the calculated distances of the ground points generated by the FMS method to the reference DEM of the USGS (North pointing to right).

The repeating linear undulations may be caused by the misalignment, Δt, between the two time-tagged datasets of the airborne lidar system: the waveform data recorded by the laser scanner, and the GPS/IMU measurement from the POS unit. The undulations can be reduced by adjusting the value of Δt, as is shown in Fig. 10. A carefully designed calibration will be conducted to optimize the final lidar products.

IV. Conclusion

In lidar measurement, the distance between the laser scanner and the target is derived from the waveform decomposition result. A suitable waveform model and decomposition algorithm is indispensable for improving the accuracy and quality of lidar products. In this work, we compared a nonparametric method and the popular parametric approach by using them to decompose lidar waveforms. In the first experiment, the simulated waveforms were generated with GMM. Both approaches returned satisfying results in that case. In the second experiment, the waveforms were acquired with a real lidar sensor. The nonparametric approach fitted the data better in terms of residuals.

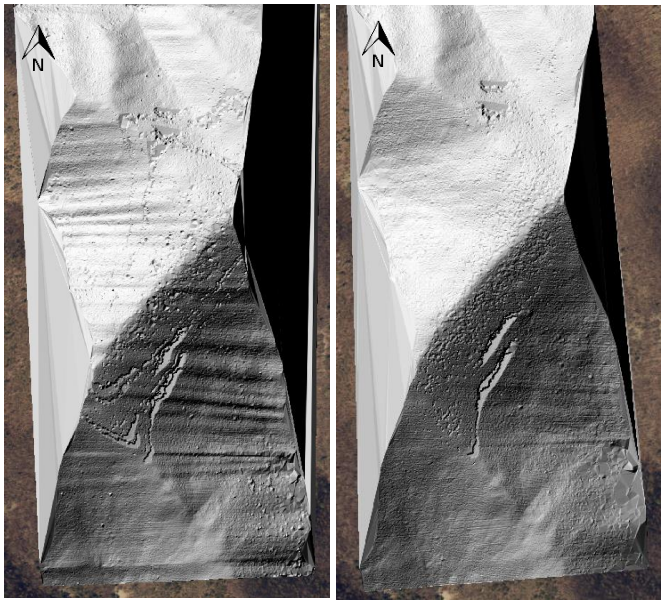

Fig. 10. Hillshaded DEMs before (left) and after (right) Δt correction

The DEMs generated from the point clouds of both methods provide higher level of detail when compared with the USGS 5m DEM. Further calibration is needed to eliminate the undulation patterns observed on both surfaces.

More interesting results are expected from the extension of the work. For the real lidar data, a more quantitative method can be applied to assess the different approaches if the ground truth is provided. The cases of multiple overlapping components can be studied if the number of detected objects is known. The work presented in this paper deserves further effort in the future.

References

[1] Shan, J., and Toth, C., 2018, Topographic Laser Ranging and Scanning: Principles and Processing, 2nd Edition, CRC Press.

[2] Mallet, C., and Bretar, F., 2009, Full-Waveform Topographic LiDAR: State-of-art, ISPRS Journal of Photogrammetry and Remote Sensing, Vol. 64, pp. 1-16.

[3] Bretar, F., Chauve, A., Mallet, C., Jutzi, B., 2008, Managing Full Waveform LiDAR Data: A Challenging Task for the Forthcoming Years, Int. Arch. Photogrammetry Remote Sensing. Spatial Inf. Sci. 37 (Part 1), pp. 415-420.

[4] Wagner, W., Roncat, A., Melzer, T., Ullrich, A., 2007, Waveform Analysis Techniques in Airborne Laser Scanning, Int. Arch. Photogrammetry Remote Sensing Spatial Inf. Sci. 36 (Part 3/W52), pp 413-418..

[5] Azadbakht, M., Fraser, S. C., and Khoshelham, K., 2016, A Sparsity-Based Regularization Approach for Deconvolution of Full-Waveform Airborne Lidar Data, Remote Sensing, Vol. 8, 648.

[6] Wu, J., Van Aardt, J. A. N., and Asner, P. G., 2011, A Comparison of Signal Deconvolution Algorithms Based on Small-Footprint Lidar Waveform Simulation, IEEE Trans. on Geoscience and Remote Sensing, Vol. 49, No. 6, pp. 2402-2414.

[7] Jung, J., and Crawford, M. M., 2008, A Two-Stage Approach for Decomposition of ICESat Waveforms, IGARSS, 2008 IEEE International, July 2008, pp. 680-683.

[8] Hernandez-Marin, S., Wallace, A. and Gibson, W., 2007, Bayesian Analysis of LiDAR Signals with Multiple Returns, IEEE Trans. on Pattern Analysis and Machine Intelligence, Vol. 29, No. 12, 2007, pp. 2170-2180.

[9] Parrish, C.E., Rogers, J.N., and Calder, B.R., 2014, Assessment of Waveform Shape Features for Lidar Uncertainty Modeling in a Coastal Salt Marsh Environment, Geoscience and Remote Sensing Letters, Vol. 11, No. 2, pp. 569-573.

[10] Li, Q., Ural, S., Anderson, J. and Shan, J., 2016, Decomposing Lidar Waveforms with Nonparametric Classification Methods, in IGARSS, 2016 IEEE International, July 2016.

[11] Hofton, M., Minster, J. and Blair. B., 2000, Decomposition of Laser Altimeter Waveforms, IEEE Trans. on Geoscience and Remote Sensing, Vol. 38, No. 4, July 2000, pp. 1989-1996.

[12] Dempster, A., Laird, N. and Rubin, D., 1977. Maximum Likelihood from Incomplete Data via the EM Algorithm, Journal of the Royal Statistical Society, Vol. 39, No. 1, pp. 1-38.

[13] Fukunaga, K., 1975, The Estimation of the Gradient of a Density Function, with Applications in Pattern Recognition, IEEE Trans. on Information Theory, Vol. IT-21. No. 1, January 1975, pp. 32-40.

[14] Li, Q., Ural, S., Anderson, J. and Shan, J., 2016, A Fuzzy Mean-Shift Approach to Lidar Waveform Decomposition, IEEE Trans. on Geoscience and Remote Sensing. Vol. 54, Issue 12, pp. 7112-7121.

[15] Chirico, P.G., 2004, LIDAR derived 5m resolution bare earth and first return digital elevation model of the Paine Run watershed, Augusta County, Virginia, Open-File Report OF-2004-1320, U.S. Geological Survey.

[16] Besl, P., and McKay, N.D., 1992, A Method for Registration of 3-D Shapes, in IEEE Trans. on Pattern Analysis and Machine Intelligence, Vol. 14, No. 2, pp. 239-256, Feb 1992.

[17] CloudCompare (version 2.8) [GPL software], (2017). Retrieved from http://www.cloudcompare.org/